Article

Dynamic Recrystallization Kinetics of As-Cast Fe-Cr-Al-La Stainless Steel during Hot Deformation

Zhenqiang Deng [1], **Jianhua Liu [1,*]**, **Jian Shao [1]** and **Alexander McLean [2,*]**

1 National Engineering Research Center for Advanced Rolling and Intelligent Manufacturing, University of Science and Technology Beijing, Beijing 100083, China; dengzhenqiang@outlook.com (Z.D.)
2 Department of Materials Science and Engineering, University of Toronto, Toronto, ON M5S 3E4, Canada
* Correspondence: liujianhua@metall.ustb.edu.cn (J.L.); amclean16@cogeco.ca (A.M.);
Tel.: +86-010-62332958-6421 (J.L.); +1-416-978-1291 (A.M.)

Abstract: To investigate the dynamic recrystallization (DRX) behavior of as-cast Fe-20Cr-5.5Al-0.64La stainless steel, a series of compression tests were carried out on a Gleeble-3500 thermal simulator in the temperature range of 1000~1150 °C and the strain rate range of 0.001~1 s^{-1}. The true stress-true strain curves were obtained and their characteristics were analyzed. Using regression analysis, the apparent activation energy for the Fe-20Cr-5.5Al-0.64La stainless steel was estimated to be 300.19 kJ/mol, and the constitutive equation was developed successfully with a hyperbolic sine equation as: $\dot{\varepsilon} = e^{21.91}[\sinh(0.035\sigma)]^{3.18}\exp\left(\frac{-300190}{RT}\right)$. The critical strain, the peak strain and the strain for the maximum softening rate were identified based on the work hardening rate curves and expressed as a function of the Zener−Hollomon parameter. The kinetic model of DRX was established using the stress−strain data. According to the analysis of the kinetics model and microstructure evolution, the evolution of DRX volume could be described as follows: the volume fraction of DRX grains increased with an increase in strain; at a fixed deformation temperature, the DRX volume fraction was larger at a lower strain rate for the same strain; and the size of DRX grains increased with an increase in temperature or a decrease in strain rate.

Keywords: FeCrAl stainless steel; hot deformation; flow behavior; dynamic recrystallization; kinetic model

1. Introduction

FeCrAl stainless steel is an ideal material for the production of internal combustion engine tail gas purifier carriers [1]. FeCrAl stainless steel foil thickness is generally 50–100 μm with a width of 300~1000 mm, which implies higher requirements for the microstructure and mechanical properties of FeCrAl stainless steel [2]. To improve the mechanical properties of FeCrAl stainless steel during the production process, many scholars have studied the final processing stage, while attention to the initial ingot is relatively limited [3,4].

To improve the oxidation resistance at a high temperature, FeCrAl stainless steel contains higher aluminum, which is usually more than 3 wt.% [5]. Due to the high content of Al and Cr, the microstructure of FeCrAl alloy is always a body-centered cubic structure during the solidification and cooling process, which prevents it from refining grains by phase transition as other mild steels do [6–9]. Hot deformation has a very important effect on the microstructure and final performance of alloys [10]. During the hot deformation process, slip, climb, multiplication and interaction of dislocations can occur, resulting in great changes in the microstructure of alloys. The DRX formed during the deformation process can improve the strength and toughness of the products through microstructure reconstruction, grain refinement and structural homogenization [11]. It is very significant to study the recrystallization of FeCrAl stainless steel to increase product yield and reduce production cost.

Many studies have shown that DRX is prone to occur in conventional austenitic stainless steels because of the low stacking fault energy, which promotes the accumulation of moving dislocations to a critical value [12–14]. The traditional idea is that the ferrite structure has a high fault energy and the mechanism of dynamic softening in hot processing is generally dynamic recovery and dynamic polygon, but not recrystallization [15,16]. However, dynamic recrystallization has been found during the hot deformation of high purity α-Fe [17,18], IF steel [19], and high Cr ferritic stainless steel [20–22] in recent years. Fei Gao et al. [23] also studied the nucleation mechanism of DRX of Cr25Ti ferritic stainless steel. It can be seen that DRX can also occur in ferritic steel under specific technological conditions. In addition, Tsuji et al. [24] found that dynamic recrystallization of ferrite grains is not uniform, and dynamic recrystallization is not easy to occur in ferrite grains with specific orientation, indicating that the angle and orientation of grains also have an effect on the dynamic recrystallization of ferrite. In a study on Fe-18Cr ferritic steel, Abedi et al. [25] also found that there are critical conditions regarding temperature and strain rate for the occurrence of dynamic recrystallization. However, studies on the hot deformation behavior of FeCrAl stainless steel and recrystallization mechanisms appear to be quite limited. Besides, the addition of La has a significant effect on the solidification microstructure and mechanical properties of the FeCrAl stainless steel. Therefore, a deep understanding of flow behavior, coupled with microstructure evolution, is very important for the accurate design of FeCrAl stainless steel forming processes.

In the present work, the flow behavior, microstructure evolution, and DRX kinetics of Fe-Cr-Al-La stainless steel under different deformation temperatures and strain rates were systematically studied with isothermal compression tests. The constitutive relationship between flow stress, strain rate and deformation temperature was developed. A DRX kinetic model of Fe-Cr-Al-La stainless steel during hot deformation was established to predict the softening behavior. The microstructure was also observed in order to investigate the DRX nucleation mechanisms.

2. Materials and Methods

A 25 kg Fe-Cr-Al-La alloy ingot was prepared using commercial purity materials in a vacuum induction furnace. Its chemical composition is listed in Table 1. As shown in Figure 1, the cylindrical specimens, the height of which is perpendicular to the columnar crystals of the ingot, were cut from the columnar zone of the ingot uniformly to ensure a homogeneous performance. The diameter and height of the specimens were 10 mm and 15 mm, respectively. The isothermal compression tests were performed on a Gleeble-3500 thermal simulator at temperatures of 1000~1150 °C with an interval of 50 °C and at strain rates of 0.001~1 s^{-1}. The cylindrical specimens were compressed axially. Temperature changes during the hot compression were monitored by a thermocouple that was welded at the mid-height of the specimens. During the tests, the specimens were first heated to 1250 °C at a rate of 5 K/s and held for 3 min to ensure homogenization. Then, they were cooled to the predetermined temperatures at a cooling speed of 10 K/s. After isothermal holding for 60 s, the specimens were hot compressed to a height reduction of 20%, 40% and 60% (true strain of 0.223, 0.511 and 0.916), respectively. All specimens were quenched in water immediately after deformation to retain their microstructure. All tests were carried out in an argon atmosphere to prevent oxidation of the samples. The variation of true stress (σ) with true strain (ε) was recorded automatically per half a second by a computer at each deformation condition during isothermal compression. After the tests, the specimens were cut symmetrically along the axis. On the cut surface, the microstructure was observed with optical microscopy after conventional polishing and etching with a chloride solution (20 g $FeCl_3$ + 30 mL HCl + 100 mL distilled water).

Table 1. Chemical composition of the Fe-Cr-Al-La alloy ingot (wt.%).

C	Si	Mn	P	S	Cr	Al	La	Fe + Others
0.042	0.28	0.19	0.0076	0.0011	19.95	5.49	0.64	balance
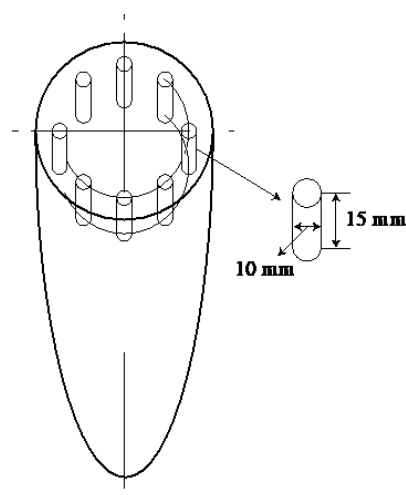
Figure 1. Schematic diagram of the sampling method for isothermal compression tests.

3. Results and Discussion

3.1. Flow Curves

Figure 2 shows the true stress−strain curves of the specimens with a 60% height reduction at various temperatures and strain rates. Except at 1000, 1050, and 1100 °C with strain rate ($\dot{\varepsilon}$) of $1\,\text{s}^{-1}$, a peak appears on each flow curve, followed by a lower flow stress, which is thought to be characteristic of the occurrence of dynamic recrystallization [26,27]. When the strain rate is less than $0.01\,\text{s}^{-1}$, the stress declines slightly after the peak points of the flow curves, which is very similar to the studies of DRX in some ferritic alloys [20,28,29]. Work hardening generally results from dislocation rising quickly as strain increases. Dynamic softening, such as DRX, may occur when strain reaches a certain level, partially offsetting the work hardening effect [26]. With an increase in strain rate and a decrease in deformation temperature, the Fe-Cr-Al-La stainless steel shows sensitivity to the changes in strain rate and deformation temperature, and the peak stress and steady flow stress increase. This inhibits DRX from taking place, and as a result, the deformed specimens exhibit more work hardening. The reason is that a higher strain rate and a lower deformation temperature will shorten the energy accumulation time and reduce the boundary mobility, leading to the hindrance of nucleation and growth of dynamic recrystallized grains and the disappearance of dislocation [30–33]. When the strain rate reaches $1\,\text{s}^{-1}$, the flow curves do not show softening at 1000, 1050, and 1100 °C.

When the strain of the specimen undergoing dynamic recrystallization is large enough, the flow stress tends to rise again. This may be caused by the significant increase in friction force between the compressed specimen and anvils due to the increase in the contact area above this strain [34].
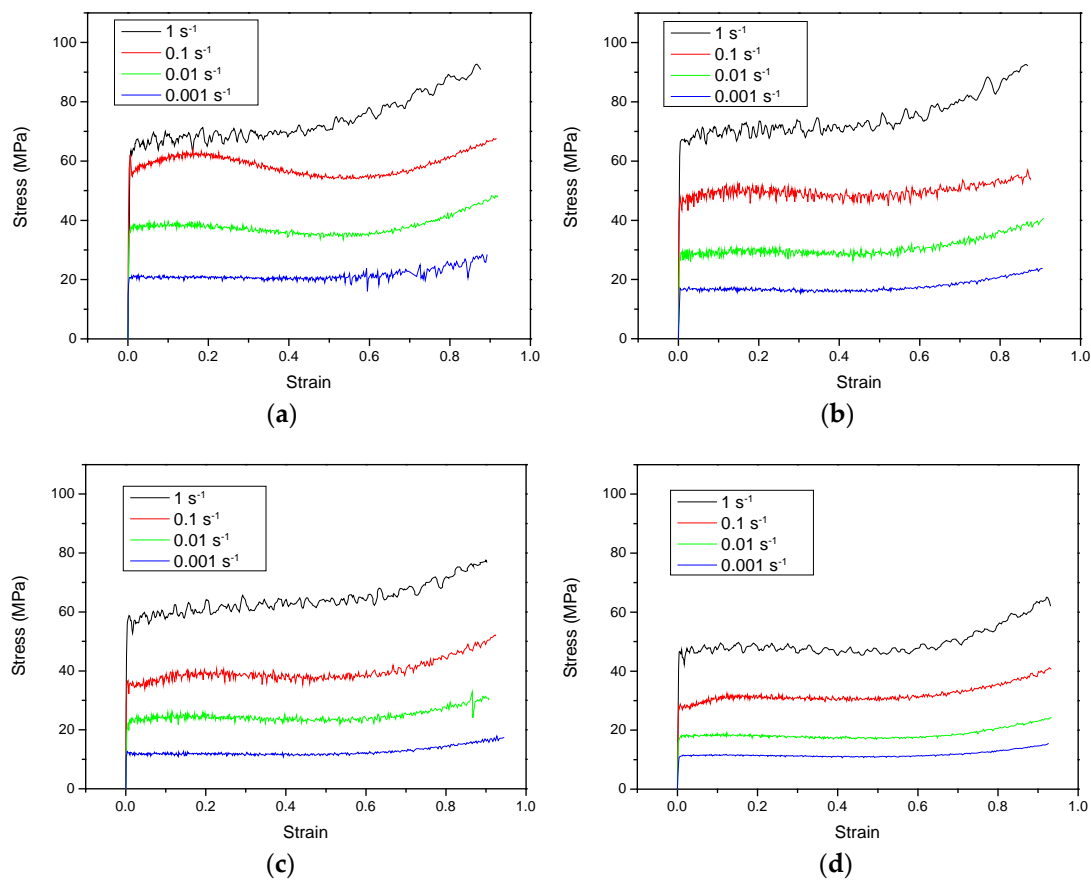
Figure 2. True stress−strain curves of the specimens which height reduction is 60% under different deformation conditions: (**a**) 1000 °C; (**b**) 1050 °C; (**c**) 1100 °C; and (**d**) 1150 °C.

3.2. Determination of DRX Characteristic Parameters

The relationship between σ and work hardening rate ($\theta = d\sigma/d\varepsilon$) can be used to calculate the critical strain and stress for the onset of DRX, which are crucial parameters for optimizing the hot working process.

According to the stress−strain curve, the curve of θ vs. σ at a strain rate of 1 s^{-1} and at 1150 °C is shown in Figure 3. Kim et al. [35,36] found that the critical stress (σ_c) and the peak stress (σ_p) divide the $\theta − \sigma$ curve into three segments. The rate of work hardening is positive in the first and second segments. In the first segment, the curve has a greater slope and decreases rapidly. When $\partial^2\theta/\partial\sigma^2 = 0$, dynamic recrystallization begins to occur, and the corresponding strain is the critical strain (ε_c) of DRX. As the strain continues to increase, θ decreases slowly in the second segment because the work hardening is partially offset by DRX. The values of σ_p and the peak strain (ε_p) can be determined at the first emergence of $\theta = 0$ [37]. In the third segment, from the peak stress to the steady state stress (σ_{ss}), the work hardening rate changes to negative, which means that the dynamic softening caused by DRX is more effective than the work hardening. The strain and stress for the maximum softening rate (ε^* and σ^*) are determined when θ decreases to the valley point in the $\theta − \sigma$ curve [38]. When θ again equals to zero, DRX develops completely, and DRX softening and work hardening are balanced.

Figure 4 shows the relationship curves between θ and σ under other experimental conditions. The same method can be used to determine the values of σ_p, σ_c, σ^* and σ_{ss} and the corresponding strain values of ε_p, ε_c, ε^* and ε_{ss}. The results are listed in Table 2.
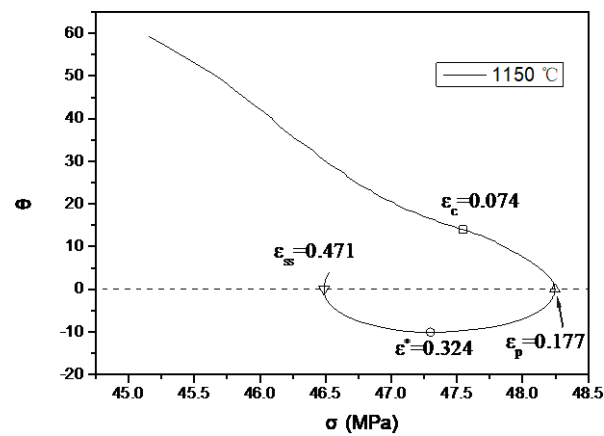
Figure 3. The curve of θ vs. σ at 1150 °C and $\dot{\varepsilon} = 1$ s^{-1}.

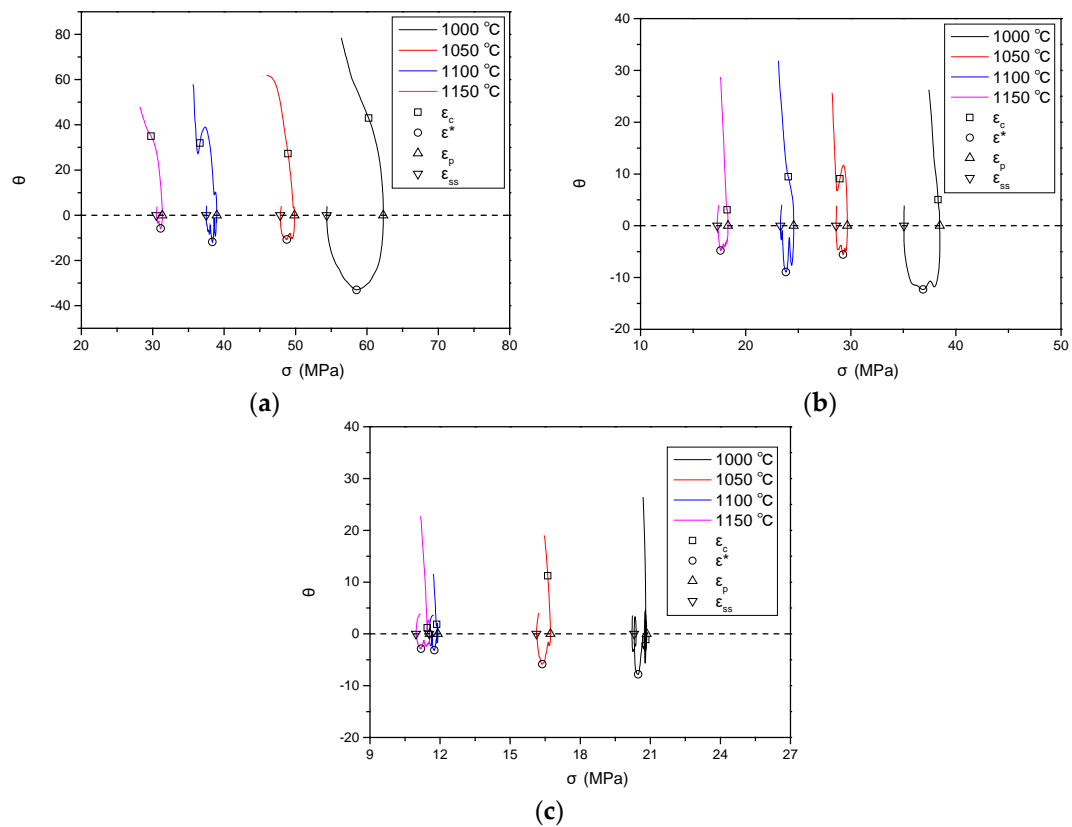**Figure 4.** θ vs. σ plots for Fe-Cr-Al-La stainless steel at strain rates of (**a**) 0.1 s^{-1}, (**b**) 0.01 s^{-1} and (**c**) 0.001 s^{-1}.

Table 2. Values of DRX characteristic parameters at different deformation conditions.

Temperature (°C)	$\dot{\varepsilon}$ (s^{-1})	σ_p (MPa)	ε_p	σ^* (MPa)	ε^*	σ_{ss} (MPa)	ε_{ss}	σ_c (MPa)	ε_c
1150	1	48.25	0.177	47.3	0.324	46.49	0.471	47.55	0.074
	0.1	31.34	0.165	31.11	0.232	30.52	0.461	29.75	0.070
	0.01	18.32	0.111	17.62	0.319	17.30	0.494	18.24	0.071
	0.001	11.56	0.11	11.12	0.316	10.97	0.494	11.46	0.051
1100	0.1	38.97	0.19	38.34	0.324	37.51	0.466	36.62	0.075
	0.01	24.57	0.169	23.84	0.319	23.31	0.496	24.05	0.078
	0.001	11.91	0.097	11.76	0.277	11.54	0.44	11.86	0.066

Table 2. *Cont.*

Temperature (°C)	$\dot{\varepsilon}$ (s^{-1})	σ_p (MPa)	ε_p	σ^* (MPa)	ε^*	σ_{ss} (MPa)	ε_{ss}	σ_c (MPa)	ε_c
	0.1	49.86	0.185	48.78	0.317	47.87	0.444	48.95	0.074
1050	0.01	29.67	0.168	29.27	0.264	28.6	0.438	28.97	0.086
	0.001	16.73	0.128	16.37	0.266	16.13	0.407	16.61	0.063
	0.1	62.3	0.163	58.56	0.326	54.37	0.542	60.23	0.076
1000	0.01	38.48	0.151	36.88	0.302	35.06	0.514	38.3	0.079
	0.001	20.84	0.155	20.48	0.315	20.22	0.468	20.81	0.056

3.3. Constitutive Equations

The constitutive equation is an important mathematical expression to describe the hot deformation behavior of materials. The constitutive equation can be used to calculate the extensions under specified loads in the process of creep and the stress at a specified strain rate in hot deformation [39]. In addition, the constitutive equation may incorporate some information related to the thermal-mechanical history and microstructure factors depending on the user's requirement [40]. The constitutive relationship between flow stress, strain rate and deformation temperature in hot deformation can be expressed by the hyperbolic sine law [41,42]:

$$\dot{\varepsilon} = A[\sinh(\alpha\sigma)]^n \exp(-Q/RT) \tag{1}$$

where σ is the flow stress (MPa), $\dot{\varepsilon}$ is the strain rate (s^{-1}), Q is the apparent activation energy for hot deformation (J/mol), R is the universal gas constant (8.314 J mol^{-1} K^{-1}), T is the deformation temperature (K), A and α are the material constants, and n is the stress exponent. The value of Q, which is influenced by the material's chemical compositions and as-received status, indicates the deformation difficulty of the alloy [43].

By taking the natural logarithms of both sides of Equation (1), the new expression can be derived:

$$\frac{Q}{RT} = \ln A - \ln\dot{\varepsilon} + n\ln\sinh(\alpha\sigma) \tag{2}$$

From Equation (2), at a constant temperature, the stress exponent (n) can be determined as the slope of $\ln\dot{\varepsilon}$ versus $\ln\sinh(\alpha\sigma)$ plot, as shown in Equation (3):

$$n = \left.\frac{\partial\ln\dot{\varepsilon}}{\partial\ln\sinh(\alpha\sigma)}\right|_T \tag{3}$$

At high and low stress levels, the relationship between flow stress and strain rate can be expressed by the power law and the exponential law (Equations (4) and (5)), respectively [16]. Equations (4) and (5) can be combined into the hyperbolic sine relation as shown in Equation (6), where $\alpha = \beta/n_1$, MPa^{-1}.

$$\dot{\varepsilon} = A_1\sigma^{n_1} \tag{4}$$

$$\dot{\varepsilon} = A_2\exp(\beta\sigma) \tag{5}$$

$$\dot{\varepsilon} = A_3[\sinh(\alpha\sigma)]^{n_2} \tag{6}$$

According to Equations (4) and (5), $n_1 = d\ln\dot{\varepsilon}/d\ln\sigma$ and $\beta = d\ln\dot{\varepsilon}/d\sigma$ (Mpa^{-1}). Some scholars [16] have shown that σ can be represented by the peak stress (σ_p) for DRX in metals. The plots of $\ln\dot{\varepsilon} - \ln\sigma_p$, $\ln\dot{\varepsilon} - \sigma_p$, and $\ln\dot{\varepsilon} - \ln\sinh(\alpha\sigma_p)$ at different temperatures, as shown in Figure 5, can be obtained by submitting the peak stress to Equations (4)–(6). The mean values of all slope rates in Figure 5a and b are accepted as the material constants n_1 and β, thus $n_1 = 4.26$, $\beta = 0.15$ MPa^{-1}, and $\alpha = \beta/n_1 = 0.035$ MPa^{-1}. In Figure 5c, the slopes of the straight lines obtained by linear regression at different temperatures are

similar, which proves that Equation (1) can correctly describe the flow curves in Figure 2. The average value of n_2 at different temperatures is then calculated as 3.17.
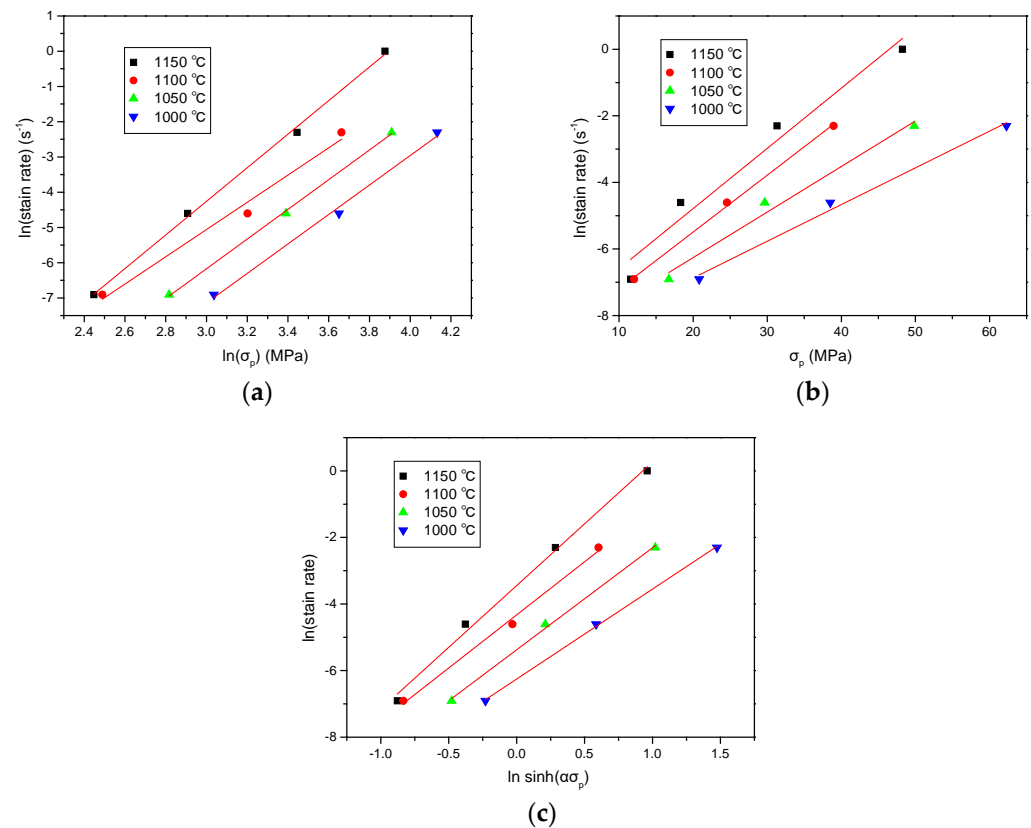

(a)

(b)

(c)

Figure 5. Relationship between peak stress and strain rate of Fe-Cr-Al-La stainless steel: (**a**) relationship of $\ln \dot{\varepsilon} - \ln \sigma_p$; (**b**) relationship of $\ln \dot{\varepsilon} - \sigma_p$; and (**c**) relationship of $\ln \dot{\varepsilon} - \ln \sinh(\alpha\sigma_p)$.

According to Equation (2), the apparent activation energy can be determined using Equation (7):

$$Q = nR \left. \frac{\partial \ln \sinh(\alpha\sigma)}{\partial(1/T)} \right|_{\dot{\varepsilon}} = R[\partial \ln \sinh(\alpha\sigma)/\partial(1/T)]_{\dot{\varepsilon}} [\partial \ln \dot{\varepsilon}/\partial \ln \sinh(\alpha\sigma)]_T \qquad (7)$$

Figure 6 shows the fitted linear relationships of $\ln \sinh(\alpha\sigma_p)$ versus $1/T$ at different strain rates. According to the data in Figure 6, under different strain rates, the mean value of all the slopes is 11.39. Q is then calculated as 300.19 kJ/mol using Equation (7).
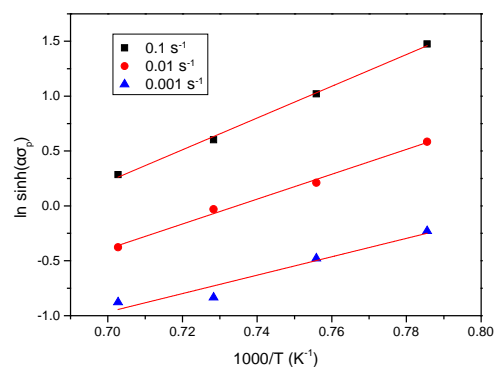

Figure 6. The linear relationship between $\ln(\sinh\alpha\sigma_p)$ and $1/T$.

The influence of temperature and strain rate on hot deformation is often described by the Zener−Holloman parameter, which can be expressed as Equation (8) [41]:

$$Z = \dot{\varepsilon} \exp\left(\frac{Q}{RT}\right) \tag{8}$$

Equation (8) can be rewritten as

$$\ln Z = \ln \dot{\varepsilon} + \frac{Q}{RT} = \ln A + n \ln \sinh(\alpha\sigma) \tag{9}$$

According to the calculated Q value, the Z parameters under different deformation conditions can be obtained with Equation (9), and the linear relationship between $\ln Z$ and $\ln \sinh(\alpha\sigma_p)$ is shown in Figure 7. The linear correlation coefficient is 0.981, which suggests that the $Z - \sigma$ hyperbolic sine model is suitable for the study on Fe-Cr-Al-La stainless steel compression deformation. The more accurate n and $\ln A$ are determined as 3.18 and 21.91, respectively.
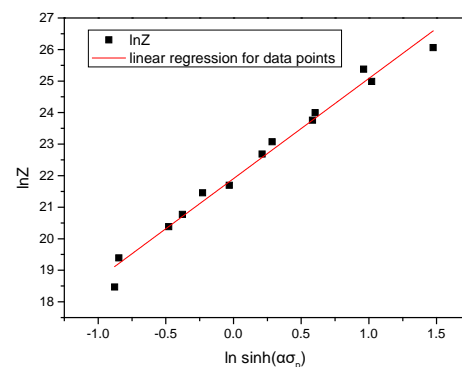

Figure 7. The relationship between $\ln Z$ and $\ln \sinh(\alpha\sigma_p)$.

With the above parameters, the constitutive equation of hot deformation of Fe-Cr-Al-La stainless steel is obtained, as shown in Equation (10).

$$\dot{\varepsilon} = e^{21.91}[\sinh(0.035\sigma)]^{3.18} \exp\left(\frac{-300190}{RT}\right) \tag{10}$$

The relation function between σ_p and the Z parameter can be calculated from Equation (10):

$$Z = \dot{\varepsilon} \exp\left(\frac{300190}{RT}\right) = e^{21.91}[\sinh(0.035\sigma_p)]^{3.18} \tag{11}$$

From Equation (1) and the definition of hyperbolic sine function, the expression of stress in hot deformation process with respect to Z parameter can be obtained:

$$\sigma = \frac{1}{\alpha} \ln\left\{ \left(\frac{Z}{A}\right)^{\frac{1}{n}} + \left[\left(\frac{Z}{A}\right)^{\frac{2}{n}} + 1 \right]^{\frac{1}{2}} \right\} \tag{12}$$

By substituting n, α and A into Equation (12), the flow stress can be written as follows:

$$\sigma = \frac{1}{0.035} \ln\left\{ \left(\frac{Z}{3.28 \times 10^9}\right)^{\frac{1}{3.18}} + \left[\left(\frac{Z}{3.28 \times 10^9}\right)^{\frac{2}{3.18}} + 1 \right]^{\frac{1}{2}} \right\} \tag{13}$$

As shown in Figure 8, the critical strain, the peak strain, the strain for the maximum softening rate and the steady state strain appear to follow a linear relationship with the Z

parameter on the double-logarithmic scale. Thus, ε_p, ε_c, ε^* and ε_{ss} can be represented as a function of Z, and their relationship can be expressed as follows:

$$\varepsilon_p = 0.0268 Z^{0.0761} \tag{14}$$

$$\varepsilon_c = 0.0282 Z^{0.0405} \tag{15}$$

$$\varepsilon^* = 0.2363 Z^{0.0104} \tag{16}$$
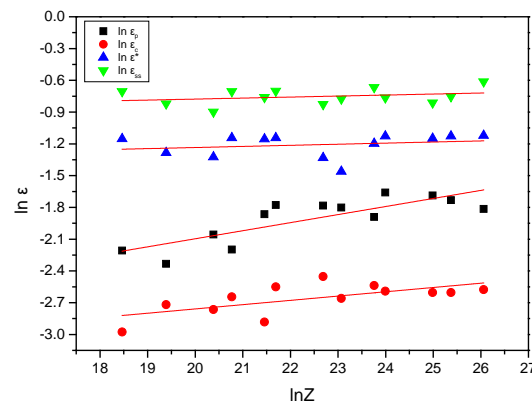
$$\varepsilon_{ss} = 0.3801 Z^{0.0095} \tag{17}$$

Figure 8. Dependences of ε_p, ε_c, ε^* and ε_{ss} on parameter Z.

3.4. DRX Kinetic Model

The dislocation density determines the occurrence of DRX. During hot deformation, when the dislocation density of the deformed material increases and accumulates to a certain extent, DRX nuclei will first form at the grain boundaries, twin boundaries and deformation bands. Dislocation multiplication caused by continuous hot deformation and dislocation disappearance caused by DRX are contradictory processes, resulting in the phenomenon of work hardening and dynamic softening, respectively. When they are in dynamic balance, the flow stress reaches a steady state, the evolution of DRX is complete, and the size of the DRX equiaxed grains formed no longer changes [44,45]. Equation (18) can be used to predict the microstructure evolution caused by DRX [38]:

$$X_{\text{DRX}} = 1 - \exp\left[-k\left(\frac{\varepsilon - \varepsilon_c}{\varepsilon^*}\right)^m\right] \tag{18}$$

where X_{DRX} is the volume fraction of dynamic recrystallized grains, and k and m are the material constants.

The effect of DRX on flow stress can be expressed as follows [46]:

$$\sigma = \sigma_p - X_{\text{DRX}}(\sigma_p - \sigma_{ss}) \tag{19}$$

Based on Equations (18) and (19), the following expressions can be obtained:

$$X_{\text{DRX}} = \frac{\sigma - \sigma_p}{\sigma_{ss} - \sigma_p} \tag{20}$$

$$\ln[-\ln(1 - X_{\text{DRX}})] = m \cdot \ln\left[\frac{(\varepsilon - \varepsilon_c)}{\varepsilon^*}\right] + \ln k \tag{21}$$

X_{DRX} can be calculated from Equation (20). m and k in Equation (21) can be obtained with the linear regression relationship between $\ln[-\ln(1 - X_{\text{DRX}})]$ and $\ln\left[\frac{(\varepsilon - \varepsilon_c)}{\varepsilon^*}\right]$.

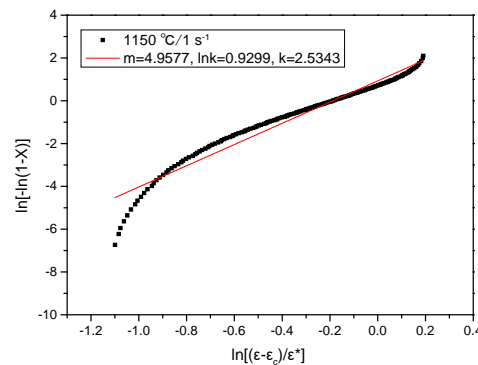As an example, the relationship between $\ln[-\ln(1 - X_{\text{DRX}})]$ and $\ln\left[\frac{(\varepsilon - \varepsilon_c)}{\varepsilon^*}\right]$ for the condition of 1150 °C and 1 s^{-1} is shown in Figure 9. According to the linear fitting relation, m and k are calculated to be 4.958 and 2.534, respectively. Therefore, the DRX kinetic model at 1150 °C and 1 s^{-1} can be expressed by the following equation:

$$\begin{cases} X_{\text{DRX}} = 0 \ (\varepsilon < \varepsilon_c) \\ X_{\text{DRX}} = 1 - \exp\left[-2.534\left(\frac{\varepsilon - 0.074}{0.324}\right)^{4.958}\right] \ (\varepsilon \geq \varepsilon_c) \end{cases} \tag{22}$$

Figure 9. The relationship between $\ln[-\ln(1 - X_{\text{DRX}})]$ and $\ln\left[\frac{(\varepsilon - \varepsilon_c)}{\varepsilon^*}\right]$ at 1150 °C and 1 s^{-1}.

The same method was used to determine the kinetic model under other conditions. Figure 10 shows the DRX kinetic curves under different conditions. As shown in Figure 10, DRX only occurs when strain exceeds the critical strain. It also shows that X_{DRX} increases with an increase in strain, and its evolution shows a growing trend of "slow-fast-slow" s-like curve [46]. The increase in X_{DRX} to one indicates that the DRX process is complete. By comparing these curves, it is found that at a specific temperature, X_{DRX} is larger at a lower strain rate for the same strain. This is because the grain boundary mobility increases with a decrease in strain rate, which accelerates the dynamic recrystallization.

3.5. Microstructure Evolution and DRX Mechanism

Figure 11 shows the DRX evolution of the Fe-Cr-Al-La stainless steel at 1000 °C and 0.1 s^{-1} according to various strains. It can be seen from Figure 11a that the original grains in the as-cast steel are very coarse. As shown in Figure 11b, serrated grain boundaries appeared when the strain is 0.223. Some fine grains are formed at the original grain boundaries and the triple junction. This means that DRX occurs under this condition [47]. The banded dislocation substructures appear inside the original grains, as indicated by the blue arrows. Figure 11c shows that more and more fine DRX grains are formed at the original grain boundaries and inside the coarse grains at a strain of 0.511. When strain increases to 0.916, dynamic recrystallization is fully developed, and the volume fraction of DRX grains (X_{DRX}) reaches one, as shown in Figure 11d. The above analysis shows that X_{DRX} increases with an increase in strain, which is in good agreement with the DRX kinetic models.

The microstructures of the Fe-Cr-Al-La stainless steel, which is compressed to the strain of 0.223 at 1150 °C and at various strain rates of 0.001~1 s^{-1}, are shown in Figure 12. The original coarse grain boundaries and DRX grains can be clearly distinguished. The dynamic recrystallization volume fraction increases with a decrease in strain rate under the given temperature and strain conditions. Figure 12a,b also prove that fine recrystallized grains initially form at the original grain boundaries.
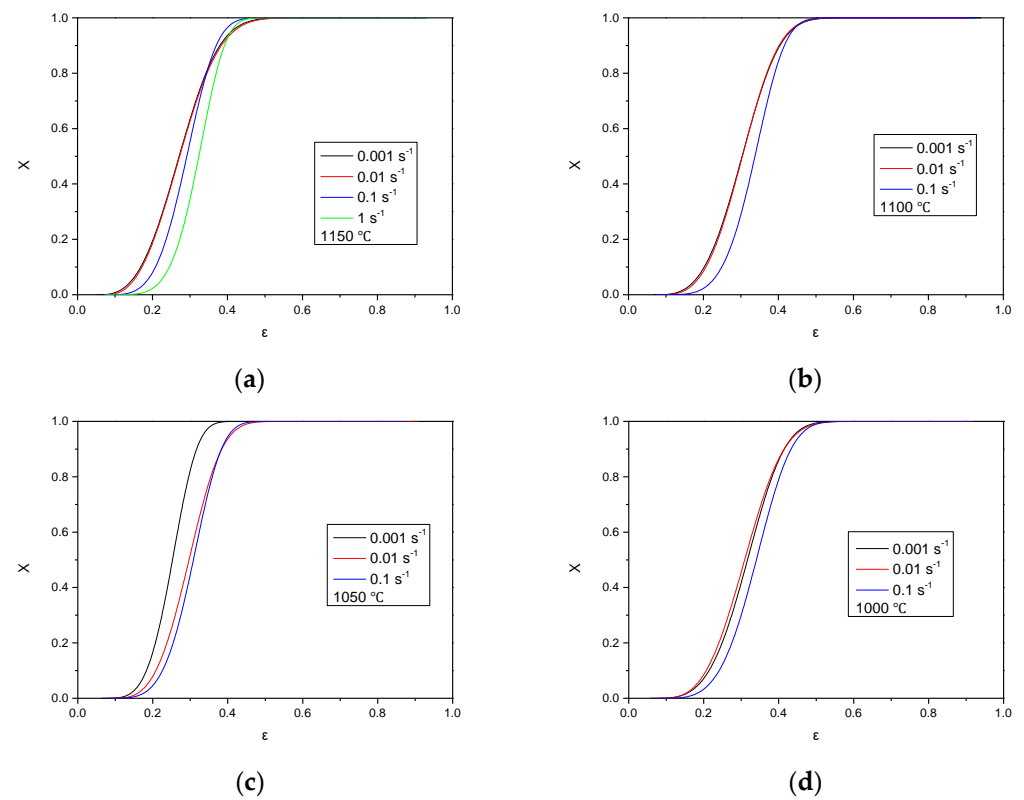
Figure 10. The curves of DRX kinetics under various conditions: (**a**) 1150 °C, (**b**) 1100 °C, (**c**) 1050 °C, and (**d**) 1000 °C.
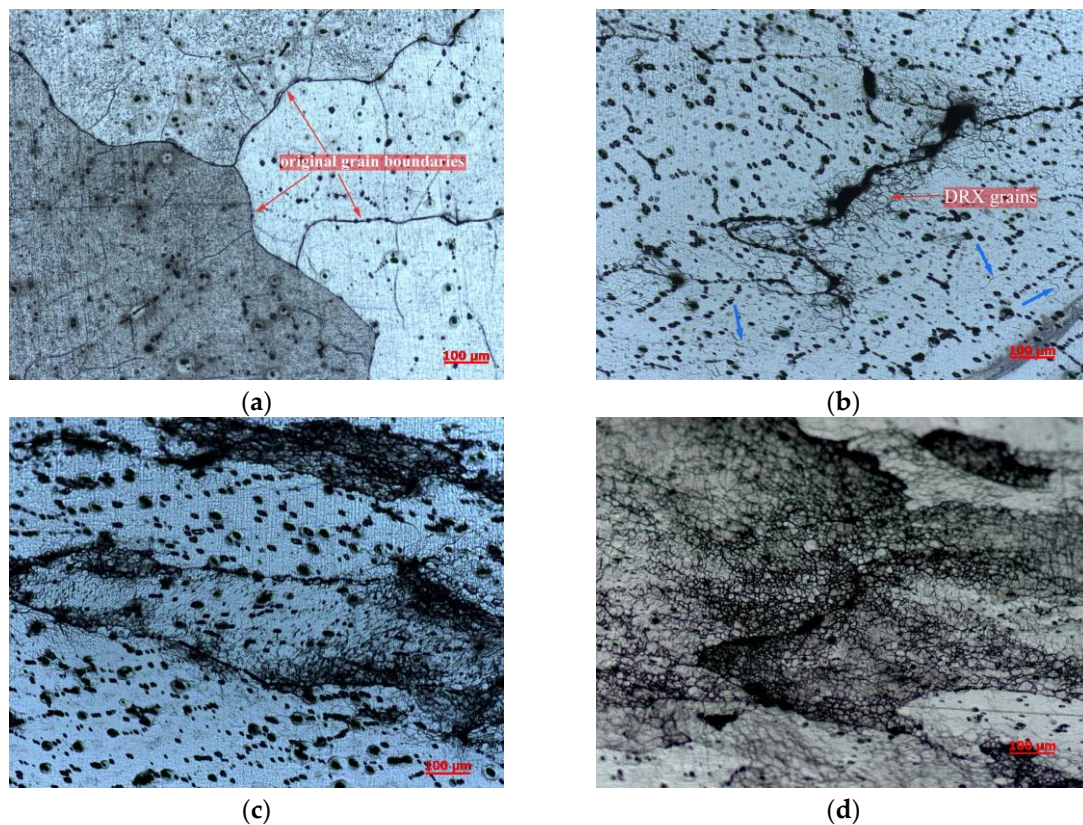

Figure 11. The DRX evolution of Fe-Cr-Al-La stainless steel at 1000 °C and 0.1 s^{-1} to various strains: (**a**) 0, (**b**) 0.223, (**c**) 0.511, and (**d**) 0.916.
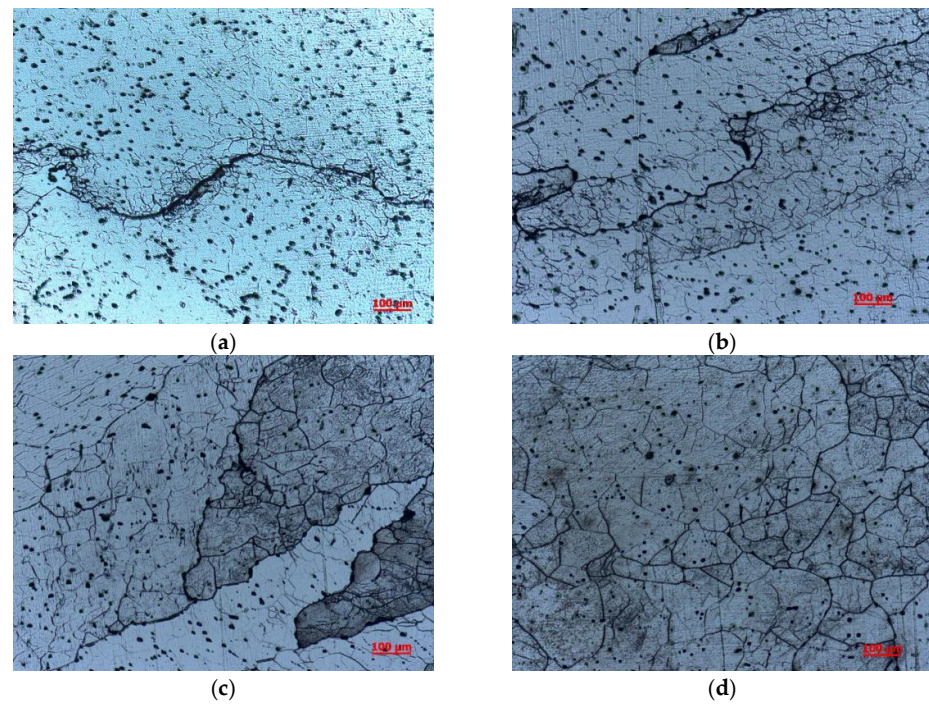
(**a**)　　　　　　　　　　　　　　　　(**b**)

(**c**)　　　　　　　　　　　　　　　　(**d**)

Figure 12. Deformation microstructure of Fe-Cr-Al-La stainless steel compressed to a strain of 0.223 at 1150 °C and at a strain rate of (**a**) 1 s^{-1}, (**b**) 0.1 s^{-1}, (**c**) 0.01 s^{-1}, and (**d**) 0.001 s^{-1}.

Figure 13 shows the deformation microstructures of the Fe-Cr-Al-La stainless steel compressed to the strain of 0.916 at a strain rate of 0.1 s^{-1} and different temperatures. It can be seen from Figures 12 and 13 that the size of dynamic recrystallization grains increases with an increase in temperature or a decrease in strain rate. This is because a higher temperature results in a higher grain boundary migration ability and a lower strain rate gives the recrystallization nucleus more time to grow [48,49].
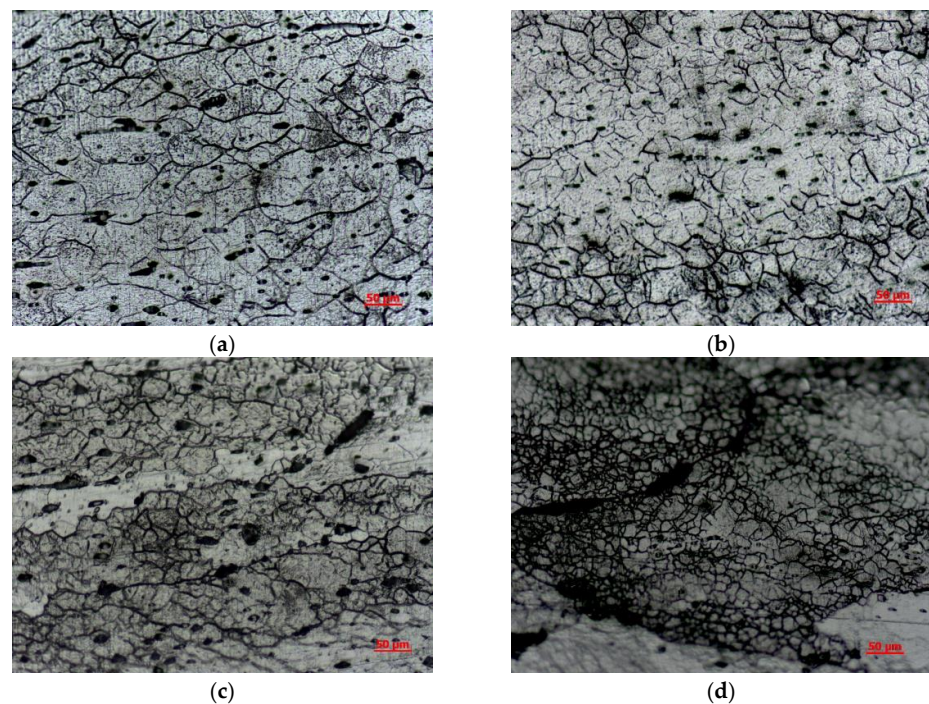

(**a**)　　　　　　　　　　　　　　　　(**b**)

(**c**)　　　　　　　　　　　　　　　　(**d**)

Figure 13. Deformation microstructure of Fe-Cr-Al-La stainless steel compressed to a strain of 0.916 at a strain rate of 0.1 s^{-1} and at (**a**) 1150 °C, (**b**) 1100 °C, (**c**) 1050 °C, and (**d**) 1000 °C.

4. Conclusions

The hot deformation behavior and dynamic recrystallization of as-cast Fe-20Cr-5.5Al-0.64La stainless steel are investigated within the deformation temperature ranging from 1000 to 1150 °C using the strain rate ranging from 0.001 to 1 s^{-1}. The following conclusions are drawn:

1. The flow stress of the Fe-Cr-Al-La stainless steel increases with a decrease in deformation temperature and an increase in strain rate. Most of the flow curves exhibit a single peak, followed by a steady-state flow, which is a typical DRX softening characteristic. The low deformation temperature and high strain rate prevent the evolution of DRX.
2. The apparent activation energy in the test conditions for the Fe-20Cr-5.5Al-0.64La stainless steel was calculated to be 300.19 kJ/mol. The constitutive equation was established with a hyperbolic sine equation by regression analysis and can be identified as: $\dot{\varepsilon} = e^{21.91}[\sinh(0.035\sigma)]^{3.18} \exp\left(\frac{-300190}{RT}\right)$ or expressed as a function of the

   Z parameter: $\sigma = \frac{1}{0.035} \ln\left\{\left(\frac{Z}{3.28\times10^9}\right)^{\frac{1}{3.18}} + \left[\left(\frac{Z}{3.28\times10^9}\right)^{\frac{2}{3.18}} + 1\right]^{\frac{1}{2}}\right\}$. The correlations

   between the critical strain, the peak strain and the strain for maximum softening rate with the Z parameter were also obtained.
3. Kinetics model of DRX was established to predict the microstructure evolution. The dynamic recrystallization kinetics at 1150 °C and 1 s^{-1} can be expressed as:
$$\begin{cases} X_{\text{DRX}} = 0 \ (\varepsilon < \varepsilon_c) \\ X_{\text{DRX}} = 1 - \exp\left[-2.534\left(\frac{\varepsilon-0.074}{0.324}\right)^{4.958}\right] \ (\varepsilon \geq \varepsilon_c) \end{cases}$$
4. Both the dynamic recrystallization kinetic model and microstructure observation show that the DRX volume fraction is larger at a lower strain rate for the same strain when the deformation temperature is fixed.
5. The microstructure observation shows that fine DRX grains initially form at the original grain boundaries. The volume fraction of DRX grains increases with an increase in strain. The microstructure observation also validated the dynamic recrystallization kinetic model. The size of dynamic recrystallization grains increases with an increase in temperature or a decrease in strain rate.

References

1. Inoue, Y.; Kikuchi, M.; Tendo, M.; Tanoue, T.; Kajimura, H. Development of Heat Resistant Stainless Steel NSSC® 21M for Catalysis Substrate of Motorcycle Muffler. *Nippon Steel Tech. Rep.* **2010**, *99*, 45–50.
2. Shen, L.; Lu, J. Overview of Researching of the Carrier Used for Automobile Gas Purfier. *Shonghai Steel Iron Res.* **2004**, *1*, 35–41.
3. Ferguson, D.; Chen, W.; Bonesteel, T.; Vosburgh, J. A Look at Physical Simulation of Metallurgical Processes, Past, Present and Future. *Mater. Sci. Eng. A* **2009**, *499*, 329–332. [CrossRef]
4. Song, R.; Ponge, D.; Raabe, D.; Speer, J.G.; Matlock, D.K. Overview of Processing, Microstructure and Mechanical Properties of Ultrafine Grained Bcc Steels. *Mater. Sci. Eng. A* **2006**, *441*, 1–17. [CrossRef]

5. Liu, F.; Halvarsson, M.; Hellström, K.; Svensson, J.E.; Johansson, L.G. First Three-Dimensional Atomic Resolution Investigation of Thermally Grown Oxide on a FeCrAl Alloy. *Oxid. Met.* **2015**, *83*, 441–451. [CrossRef]

6. He, Y.; Liu, J.; Han, Z.; Deng, Z.; Su, X.; Ji, Y. Phase Transformation and Precipitation during Solidification of FeCrAl Alloy for Automobile Exhaust Gas Purifying Systems. *J. Alloys Compd.* **2017**, *714*, 251–257. [CrossRef]

7. Deng, Z.Q.; Liu, J.H.; He, Y.; Han, Z.B.; Su, X.F.; Ding, H. Phase Transformations and Precipitation Behavior in FeCrAl Stainless Steel during Equilibrium Solidification. *Gongcheng Kexue Xuebao/Chin. J. Eng.* **2017**, *39*, 710–720. [CrossRef]

8. Deng, Z.; Liu, J.; He, Y.; Yang, Y.; McLean, A. Study on Phase Transition and Precipitation Behavior of Fecral Stainless Steel during Equilibrium Solidification. In *AISTech-Iron and Steel Technology Conference Proceedings*; AIST: Tokyo, Japan, 2019; Volume 2019, pp. 2311–2318. [CrossRef]

9. Gao, F.; Yu, F.X.; Liu, F.T.; Liu, Z.Y. Hot Deformation Behavior and Flow Stress Prediction of Ultra Purified 17% Cr Ferritc Stainless Steel Stabilized with Nb and Ti. *J. Iron Steel Res. Int.* **2015**, *22*, 827–836. [CrossRef]

10. Lin, Y.C.; Chen, X.M. A Critical Review of Experimental Results and Constitutive Descriptions for Metals and Alloys in Hot Working. *Mater. Des.* **2011**, *32*, 1733–1759. [CrossRef]

11. Wang, Z.; Fu, W.; Sun, S.; Li, H.; Lv, Z.; Zhao, D. Mechanical Behavior and Microstructural Change of a High Nitrogen Crmn Austenitic Stainless Steel during Hot Deformation. *Metall. Mater. Trans. A Phys. Metall. Mater. Sci.* **2010**, *41*, 1025–1032. [CrossRef]

12. Mandal, S.; Bhaduri, A.K.; Sarma, V.S. Role of Twinning on Dynamic Recrystallization and Microstructure during Moderate to High Strain Rate Hot Deformation of a Ti-Modified Austenitic Stainless Steel. *Metall. Mater. Trans. A Phys. Metall. Mater. Sci.* **2012**, *43*, 2056–2068. [CrossRef]

13. Mataya, M.C.; Perkins, C.A.; Thompson, S.W.; Matlock, D.K. Flow Stress and Microstructural Evolution during Hot Working of Alloy 22Cr-13Ni-5Mn-0.3N Austenitic Stainless Steel. *Metall. Mater. Trans. A Phys. Metall. Mater. Sci.* **1996**, *27*, 1251–1266. [CrossRef]

14. Mandal, S.; Bhaduri, A.K.; Subramanya Sarma, V. A Study on Microstructural Evolution and Dynamic Recrystallization during Isothermal Deformation of a Ti-Modified Austenitic Stainless Steel. *Metall. Mater. Trans. A Phys. Metall. Mater. Sci.* **2011**, *42*, 1062–1072. [CrossRef]

15. McQueen, H.J.; Bourell, D.L. Hot Workability of Metals and Alloys. *Jom* **1987**, *39*, 28–35. [CrossRef]

16. Ryan, N.D.; McQueen, H.J. Effects of Alloying upon the Hot Workability of Carbon, Microalloyed, Tool, and Austenitic Stainless Steels. *J. Mech. Work. Technol.* **1986**, *12*, 279–296. [CrossRef]

17. Glover, G.; Sellars, C.M. Recovery and Recrystallization during High Temperature Deformation of α-Iron. *Metall. Trans.* **1973**, *4*, 765–775. [CrossRef]

18. Glover, G.; Sellars, C. Static Recrystallization after Hot Deformation of α Iron. *Metall. Trans.* **1972**, *3*, 2271–2280. [CrossRef]

19. Najafi-Zadeh, A.; Jonas, J.J.; Yue, S. Effect of Dynamic Recrystallization on Grain Refinement of IF Steels. *Mater. Sci. Forum* **1993**, *113–115*, 441–446. [CrossRef]

20. Gao, F.; Yourong, X.U.; Song, B.; Xia, K. Substructural Changes during Hot Deformation of an Fe-26Cr Ferritic Stainless Steel. *Metall. Mater. Trans. A Phys. Metall. Mater. Sci.* **2000**, *31*, 21–27. [CrossRef]

21. Yagi, H.; Tsuji, N.; Saito, Y. Dynamic Recrystallization in 18%Cr Ferritic Steel. *Tetsu—Hagane/J. Iron Steel Inst. Japan* **2000**, *86*, 349–356. [CrossRef]

22. Zhu, Y.-Y.; Ning, L.-K.; Xin, T.-Z.; Liu, E.-Z.; Tong, J.; Tan, Z.; Zhou, Y.-T.; Zheng, Z. Hot Deformation Behavior and Microstructure Evolution of an Fe–30Cr–2Mo Ultra-Pure Super Ferritic Stainless Steel. *J. Iron Steel Res. Int.* **2021**, *28*, 1291–1304. [CrossRef]

23. Cao, Y.; Di, H.; Zhang, J.; Ma, T.; Zhang, J. Research on Hot Deformation Behavior and Hot Workability of Alloy 800H. *Jinshu Xuebao/Acta Metall. Sin.* **2013**, *49*, 811–821. [CrossRef]

24. Tsuji, N.; Matsubara, Y.; Saito, Y. Dynamic Recrystallization of Ferrite in Interstitial Free Steel. *Scr. Mater.* **1997**, *37*, 477–484. [CrossRef]

25. Abedi, H.R.; Zarei Hanzaki, A.; Liu, Z.; Xin, R.; Haghdadi, N.; Hodgson, P.D. Continuous Dynamic Recrystallization in Low Density Steel. *Mater. Des.* **2017**, *114*, 55–64. [CrossRef]

26. Han, Y.; Liu, G.; Zou, D.; Liu, R.; Qiao, G. Deformation Behavior and Microstructural Evolution of As-Cast 904L Austenitic Stainless Steel during Hot Compression. *Mater. Sci. Eng. A* **2013**, *565*, 342–350. [CrossRef]

27. El Wahabi, M.; Cabrera, J.M.; Prado, J.M. Hot Working of Two AISI 304 Steels: A Comparative Study. *Mater. Sci. Eng. A* **2003**, *343*, 116–125. [CrossRef]

28. Han, K.S.; Song, T.J.; De Cooman, B.C. Hot Deformation Behavior of Fe-2%Si. *ISIJ Int.* **2013**, *53*, 294–303. [CrossRef]

29. Tsuji, N.; Shinmiya, T.; Saito, Y.; Muraki, M. Deformation Microstructure and Nucleation of Recrystallization in Hot-Deformed Single Crystals of 18% Cr Ferritic Steel. *ISIJ Int.* **1998**, *38*, 380–389. [CrossRef]

30. Yue, C.-X.; Zhang, L.-W.; Liao, S.-L.; Pei, J.-B.; Gao, H.-J.; Jia, Y.-W.; Lian, X.-J. Research on the Dynamic Recrystallization Behavior of GCr15 Steel. *Mater. Sci. Eng. A* **2009**, *499*, 177–181. [CrossRef]

31. Yang, X.; Ji, Z.; Miura, H.; Sakai, T. Dynamic Recrystallization and Texture Development during Hot Deformation of Magnesium Alloy AZ31. *Trans. Nonferrous Met. Soc. China* **2009**, *19*, 55–60. [CrossRef]

32. Zheng, Q.G.; Ying, T.; Jie, Z. Dynamic Softening Behaviour of AZ80 Magnesium Alloy during Upsetting at Different Temperatures and Strain Rates. *Proc. Inst. Mech. Eng. Part B J. Eng. Manuf.* **2010**, *224*, 1707–1716. [CrossRef]

33. Petkovic, R.A.; Luton, M.J.; Jonas, J.J. Recovery and Recrystallization of Polycrystalline Copper after Hot Working. *Acta Metall.* **1979**, *27*, 1633–1648. [CrossRef]

34. Wang, X.; Liu, Z.; Luo, H. Complicated Interaction of Dynamic Recrystallization and Precipitation During Hot Deformation of Ultrahigh-Strength Stainless Steel. *Metall. Mater. Trans. A Phys. Metall. Mater. Sci.* **2016**, *47*, 6248–6258. [CrossRef]

35. Kim, S.-I.; Lee, Y.; Lee, D.L.; Yoo, Y.C. Modeling of AGS and Recrystallized Fraction of Microalloyed Medium Carbon Steel during Hot Deformation. *Mater. Sci. Eng. A* **2003**, *355*, 384–393. [CrossRef]

36. Kim, S.-I.; Yoo, Y.-C. Dynamic Recrystallization Behavior of AISI 304 Stainless Steel. *Mater. Sci. Eng. A* **2001**, *311*, 108–113. [CrossRef]

37. Mirzadeh, H.; Cabrera, J.M.; Najafizadeh, A. Modeling and Prediction of Hot Deformation Flow Curves. *Metall. Mater. Trans. A Phys. Metall. Mater. Sci.* **2012**, *43*, 108–123. [CrossRef]

38. Xu, Y.; Hua, L.; Sun, Y. Deformation Behaviour and Dynamic Recrystallization of AZ61 Magnesium Alloy. *J. Alloys Compd.* **2013**, *580*, 262–269. [CrossRef]

39. McQueen, H.J.; Ryan, N.D. Constitutive Analysis in Hot Working. *Mater. Sci. Eng. A* **2002**, *322*, 43–63. [CrossRef]

40. Samantaray, D.; Mandal, S.; Bhaduri, A.K.; Venugopal, S.; Sivaprasad, P.V. Analysis and Mathematical Modelling of Elevated Temperature Flow Behaviour of Austenitic Stainless Steels. *Mater. Sci. Eng. A* **2011**, *528*, 1937–1943. [CrossRef]

41. Sellars, C.M.; Tegart, W.J.M. Hot Workability. *Int. Metall. Rev.* **1972**, *17*, 1–24. [CrossRef]

42. Sellars, C.M.; McTegart, W.J. On the Mechanism of Hot Deformation. *Acta Metall.* **1966**, *14*, 1136–1138. [CrossRef]

43. Quan, G.-Z.; Wu, D.-S.; Luo, G.-C.; Xia, Y.-F.; Zhou, J.; Liu, Q.; Gao, L. Dynamic Recrystallization Kinetics in α Phase of As-Cast Ti–6Al–2Zr–1Mo–1V Alloy during Compression at Different Temperatures and Strain Rates. *Mater. Sci. Eng. A* **2014**, *589*, 23–33. [CrossRef]

44. Jia, J.; Zhang, K.; Lu, Z. Dynamic Recrystallization Kinetics of a Powder Metallurgy Ti-22Al-25Nb Alloy during Hot Compression. *Mater. Sci. Eng. A* **2014**, *607*, 630–639. [CrossRef]

45. Yang, Z.; Guo, Y.C.; Li, J.P.; He, F.; Xia, F.; Liang, M.X. Plastic Deformation and Dynamic Recrystallization Behaviors of Mg-5Gd-4Y-0.5Zn-0.5Zr Alloy. *Mater. Sci. Eng. A* **2008**, *485*, 487–491. [CrossRef]

46. Liu, J.; Cui, Z.; Ruan, L. A New Kinetics Model of Dynamic Recrystallization for Magnesium Alloy AZ31B. *Mater. Sci. Eng. A* **2011**, *529*, 300–310. [CrossRef]

47. Ponge, D.; Gottstein, G. Necklace Formation during Dynamic Recrystallization: Mechanisms and Impact on Flow Behavior. *Acta Mater.* **1998**, *46*, 69–80. [CrossRef]

48. Medina, S.F.; Hernandez, C.A. General Expression of the Zener-Hollomon Parameter as a Function of the Chemical Composition of Low Alloy and Microalloyed Steels. *Acta Mater.* **1996**, *44*, 137–148. [CrossRef]

49. Rollett, A.; Humphreys, F.; Rohrer, G.S.; Hatherly, M. *Recrystallization and Related Annealing Phenomena*, 2nd ed.; Pergamon: Oxford, UK, 2004; ISBN 9780080441641.